# Interface energy band alignment at the all-transparent p-n heterojunction based on NiO and $BaSnO_3$

# Interface energy band alignment at the all-transparent p-n heterojunction based on NiO and $BaSnO_3$

Jiaye Zhang, Shaobo Han, Weihuang Luo, Shuhuai Xiang, Jianli Zou, Freddy E. Oropeza, Meng Gu, and Kelvin H. L. Zhang

Citation: Appl. Phys. Lett. **112**, 171605 (2018); doi: 10.1063/1.5029422
View online: https://doi.org/10.1063/1.5029422
View Table of Contents: http://aip.scitation.org/toc/apl/112/17
Published by the American Institute of Physics

# Interface energy band alignment at the all-transparent p-n heterojunction based on NiO and $BaSnO_3$

Jiaye Zhang,[1] Shaobo Han,[2] Weihuang Luo,[1] Shuhuai Xiang,[2] Jianli Zou,[2] Freddy E. Oropeza,[3] Meng Gu,[2] and Kelvin H. L. Zhang[1,4,a)]

[1]*College of Chemistry and Chemical Engineering, Xiamen University, Xiamen 361005, China*
[2]*Department of Materials Science and Engineering, Southern University of Science and Technology, No. 1088 Xueyuan Blvd, Shenzhen, Guangdong 518055, China*
[3]*Department of Chemical Engineering and Chemistry, Technische Universiteit Eindhoven, 5600 MB, Netherlands*
[4]*Department of Materials Science and Metallurgy, University of Cambridge, 27 Charles Babbage Road, Cambridge CB3 0FS, United Kingdom*

(Received 14 March 2018; accepted 5 April 2018; published online 24 April 2018)

Transparent oxide semiconductors hold great promise for many optoelectronic devices such as transparent electronics, UV-emitting devices, and photodetectors. A *p-n* heterojunction is the most ubiquitous building block to realize these devices. In this work, we report the fabrication and characterization of the interface properties of a transparent heterojunction consisting of *p*-type NiO and *n*-type perovskite $BaSnO_3$. We show that high-quality NiO thin films can be epitaxially grown on $BaSnO_3$ with sharp interfaces because of a small lattice mismatch (∼1.3%). The diode fabricated from this heterojunction exhibits rectifying behavior with a ratio of 500. X-ray photoelectron spectroscopy reveals a type II or "staggered" band alignment with valence and conduction band offsets of 1.44 eV and 1.86 eV, respectively. Moreover, a large upward band bending potential of 0.90 eV for $BaSnO_3$ and a downward band bending potential of 0.15 eV for NiO were observed in the interface region. Such electronic properties have important implication for optoelectronic applications as the large built-in potential provides favorable energetics for photo-generated electron-hole separation/migration. *Published by AIP Publishing.* https://doi.org/10.1063/1.5029422

Transparent oxide semiconductors (TOSs), with tunable electrical conductivity and high optical transparency, hold great promise for a wide range of optoelectronic applications, such as flat-panel displays, transparent field effect transistors, ultra-violet (UV) light-emitting diodes, lasers, and UV photodetectors.[1–3] A p-n heterojunction is the most ubiquitous building block to realize these devices.[4] Moreover, the device performance depends crucially on the energy band alignment and built-in potentials at the interface.[5–7] Thereby, a microscopic understanding of the atomic structures and electronic properties at the heterointerface is the most fundamental step for a better control of the performance.[8,9]

In this work, we report the fabrication of the transparent p-n heterojunction consisting of NiO and $BaSnO_3$ (BSO) and a detailed investigation of their interfacial electronic structures using high resolution X-ray photoemission spectroscopy (XPS). BSO is a transparent *n*-type semiconductor that has drawn significant attention in oxide electronics in recent years.[10,11] It crystallizes into a perovskite structure [see Fig. 1(a)], in which the $Sn^{4+}$ cation is connected to six oxygen molecules in a perfect octahedron. BSO has a large indirect bandgap of 3.2 eV and a direct bandgap of 3.5 eV and is thereby highly transparent in the visible spectrum. The conduction band minimum (CBM) is predicted to be of primarily Sn 5*s* derived states, giving rise to a dispersive band with a low electron effective mass.[12,13] The CBM also lies low in energy with respect to the vacuum level, thereby ensuring excellent *n*-type doping.[14] Indeed, La-doped BSO bulk single crystals have been shown to exhibit a room-temperature mobility of 320 $cm^2\ V^{-1}\ s^{-1}$, the highest value among all the metal oxides.[15,16] Such a high mobility was described to arise from the large dispersive Sn 5*s* derived conduction band (CB) states.[17,18] These intrinsic superior properties render BSO of considerable interest as a promising earth-abundant alternative to industry standard $In_2O_3$ based transparent electrodes and also as a new platform for fabricating high performance transparent *p-n* diodes,[10,19–21] field effect transistors,[10,22–24] and an electron transporting layer in organic perovskite solar cells.[25] Chambers *et al.*[26] found a favorable conduction band offsets at the interfaces of BSO with $SrTiO_3$ and $LaAlO_3$, opening up the possibility of achieving 2-dimensinal electron gas by modulation doping and polar discontinuity doping. Recently, Kim *et al.*[19] fabricated all-transparent *p*-CuI/*n*-BSO heterojunctions which exhibit a large rectification ratio of $6.75 \times 10^5$. However, the poor chemical stability of CuI presents a significant challenge for thin-film synthesis and device integration. It would be worthwhile to integrate BSO with existing *p*-type TOS.

However, contrary to the *n*-type counterparts, high-performance *p*-type TOSs are very limited mainly due to the localized nature of the O 2*p*-derived valence band (VB) in most oxides.[27] NiO has a wide bandgap in the range of 3.4–4 eV and becomes a *p*-type semiconductor by the formation of Ni vacancies or $Li^+$ doping.[28–30] It has been widely used as *p*-layers in oxide *p-n* heterojunction devices such as current rectifiers,[31–33] thin film field effect transistors,[34] UV photodetectors,[35] and light emitting diodes.[36] The integration

a)Email: Kelvinzhang@xmu.edu.cn

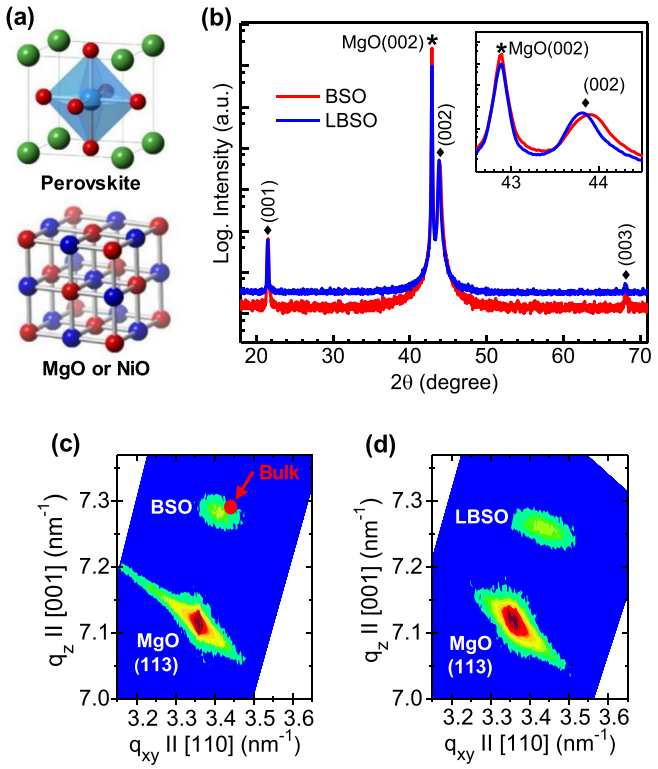


FIG. 1. (a) Perovskite and rock-salt crystal structure. (b) XRD $\theta$-$2\theta$ scans of BSO and LBSO grown on MgO(001); the inset shows detailed scans around the MgO (002) reflection (* for reflection peaks from MgO and ◆ for peaks from perovskite). (c) and (d) RSMs for BSO and LBSO around MgO(113) reflection, respectively.

of NiO with BSO will readily form an all-oxide transparent *p-n* heterojunction. Furthermore, NiO has a rocksalt crystal structure with lattice constant $a_{NiO} = 4.175$ Å, and the perovskite BSO has a lattice constant of $a_{BSO} = 4.116$ Å [Fig. 1(a)]. There is only −1.3% lattice mismatch. Therefore, it is expected that NiO can form more coherent interfaces with BSO, in comparison to other *p-n* heterojunctions such as *p*-type Cu$MO_2$ delafossites and CuI. These promises motivated us to fabricate *p-n* heterojunctions using NiO and BSO. To this end, we first grew BSO and 3% La doped $BaSnO_3$ (LBSO) epitaxial films on MgO(001) substrates by pulsed laser deposition (PLD) from respective targets (see supplementary material for detailed experiments).

We choose MgO as a substrate because it has a small lattice mismatch of −2.3% with BSO and a large bandgap with high transparency. Subsequently, high-quality NiO thin films can be epitaxially grown on BSO with sharp interfaces. The energy band alignment at the interface was studied by XPS, revealing a "staggered" band alignment with a valence band offset of 1.44 eV and a large upward band bending potential of 0.90 eV for BSO. Such interfacial electronic properties would provide favorable energetics for separation and transport of electron-hole carriers in optoelectronic applications.

BSO and LBSO films were epitaxially grown on (001)-oriented MgO substrates by PLD. MgO adopts a rocksalt crystal structure with $a_{MgO} = 4.212$ Å; perovskite BSO has a lattice constant of $a_{BSO} = 4.116$ Å [Fig. 1(a)]. There is a −2.3% lattice mismatch. Figure 1(b) shows a wide range of XRD $\theta$-$2\theta$ out-of-plane scans of 150 nm thick BSO and LBSO on MgO(001). Reflections from (002) of MgO and (00*l*) of perovskite are observed, confirming the cube-on-cube epitaxy. Reciprocal space maps (RSM) around (113) reflections of MgO shown in Figs. 1(c) and 1(d) indicate that the in-plane strain is nearly relaxed for both BSO and LBSO. The inset in Fig. 1(b) shows detailed scans around the (002) reflections. It is interesting to note the out-of-plane lattice constant of LBSO is slightly larger than that of BSO although $La^{3+}$ has a much smaller ionic radius (1.17 Å) than that of $Ba^{2+}$ (1.49 Å).[37] A similar behaviour has also been observed in bulk materials[15] and thin films grown on other substrates.[38] The expansion of the lattice parameter can be attributed to the bond-length increase between Sn and O resulted from the electron occupation of the Sn5*s*-O2*p* $\sigma$* antibonding state with La doping.

The optical and electronic properties of BSO and LBSO films on MgO(001) were characterized by UV-vis absorption spectroscopy and high-resolution XPS. Figure 2(a) shows that both films have an averaged transmission of >80% in the visible spectral region (1.8–3.1 eV). The reduced transmission in the infrared region for LBSO is due to plasmon reflection by free electrons induced by La doping. BSO was predicted to be an indirect bandgap semiconductor. The CBM is located at the Γ point with highly dispersive Sn 5*s* orbitals, while valence band maximum (VBM) is located at the *R* point of predominant O 2*p* characters.[39] We used Tauc plots of $(\alpha h\gamma)^2$ vs $h\gamma$ in Fig. 2(b) to extract the direct bandgap ($E_g^{dir}$) and $(\alpha h\gamma)^{1/2}$ vs $h\gamma$ in Fig. 2(c) for the indirect bandgap ($E_g^{ind}$), where $\alpha$ is the absorption coefficient and $h\gamma$ is the photon energy. The resulting $E_g^{dir}$ for BSO and LBSO is 3.57 eV and 3.91 eV and $E_g^{ind}$ for BSO and LBSO is 3.23 eV and 3.50 eV, respectively. The increased $E_g^{dir}$ and $E_g^{ind}$ for LBSO are attributed to the CB filling by free electrons, i.e., Burstein-Moss shift,[40] as further confirmed by XPS valence band (VB) spectra [Fig. 2(d)] described below.

The XPS VB spectra of BSO and LBSO are shown in Fig. 2(d). The energy scale is referenced to the Fermi energy ($E_F$). The VB for BSO is dominated by O 2*p* derived states at 3–9 eV and the Sn 5*s* bonding state at ∼11 eV.[39,41] No

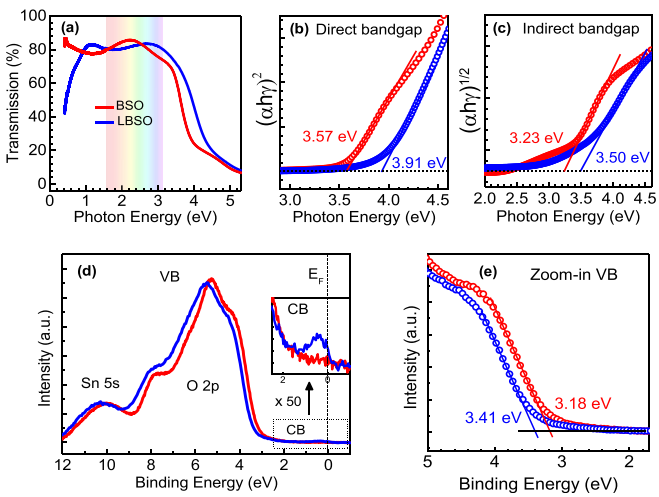


FIG. 2. Optical and electronic properties of BSO and LBSO: (a) optical transmission; (b) direct and (c) indirect bandgaps increase with La doping because of the occupation of the conduction band; (d) valence band spectra by XPS; and (e) VBM positions.

detectable intensity is observed at $E_F$ for BSO [see inset Fig. 2(d)], consistent with the highly resistive nature of the undoped film. The VBM position is determined to be at 3.18 eV below the $E_F$ for BSO by linear extrapolation of the leading edge of the VB to the baseline, as shown in Fig. 2(e). A well-defined CB feature straddling $E_F$ is observed for LBSO [inset of Fig. 2(d)], and the VBM is at 3.41 eV below $E_F$ [Fig. 2(e)], as expected due to the filling of the CB by free electrons from La doping. The Hall measurement indicates that both BSO and LBSO are *n*-type semiconductors with carrier concentrations of $n = 3 \times 10^{17}\,\mathrm{cm}^{-3}$ and $n = 2 \times 10^{20}\,\mathrm{cm}^{-3}$, respectively. The low carrier concentration in BSO might result from adventitious donor defects, most probably oxygen vacancies.[42,43] Using the carrier concentrations determined by the Hall measurement and an effective electron mass $m^*$ of $0.4m_0$,[15,44] we can estimate that $E_F$ is positioned at 0.13 eV below the CBM for BSO, while 0.31 eV above the CBM for LBSO.[45,46] Therefore, using the XPS VBM position, the $E_g^{ind}$ value for BSO should be around (3.18 + 0.13) eV. This further confirms the $E_g^{ind}$ value of 3.23 eV determined by our optical absorption. It should be noted that there is disagreement regarding the values of $E_g^{ind}$ of BSO. A value of 2.9 eV has been reported for bulk single crystals[26] and epitaxial thin films grown on $SrTiO_3$[26] based on optical absorption measurements, while 3.2 eV has been reported for BSO bulk powders[47] and epitaxial films on $SrTiO_3$ based on photoemission VB[41] and PBE calculations.[18] The scattered values might be caused by extrinsic factors such as strains resulting from epitaxial growth,[48] CB band filling by adventitious donors (e.g., oxygen vacancies),[42,43] or limitation of the measurements. Here, we emphasize that the exact value of $E_g^{ind}$ has important implication for the possibility of *p*-type doping in BSO since the $E_g^{ind}$ value reflects the band dispersion at the VBM, i.e., a high dispersion gives rise to a higher hole mobility.[49,50] A notable example is the bandgap issue of $In_2O_3$. For many years, $In_2O_3$ had been thought to have an $E_g^{ind}$ of 2.69 eV and an $E_g^{dir}$ of 3.75 eV.[51] The difference in $E_g^{dir}$ and $E_g^{ind}$ requires 1.06 eV dispersion at the VBM, which is apparently not possible considering that the VBM is mostly composed of O 2*p* orbitals.[52] Recently, it was shown that $In_2O_3$ actually has a direct but dipole forbidden bandgap of ~2.9 eV; there is no much dispersion at the VBM.[53,54]

NiO was epitaxially grown on BSO as *p*-type layers to form a *p-n* heterojunction. The XRD $\theta$-$2\theta$ scan in Fig. 3(a) and RSM in Fig. 3(b) indicate very good epitaxial growth of NiO on BSO because of the very close lattice parameter between NiO ($a_{NiO} = 4.175$ Å) and BSO. Cross-sectional STEM measurements were performed to further examine the atomic structure in the interface region of NiO/BSO. The low-magnified image shown in Fig. 3(c) confirms that the ordered NiO film form a well-defined interface with BSO. Figure 3(d) shows an atomic-resolution high-angle annular dark-field (HAADF) image viewed down to the [100] zone axis direction. Due to the low atomic number of NiO compared to BSO, the NiO region appears to be much darker than BSO in the HAADF Z-contrast image. NiO is in very good epitaxial relation with BSO; there are no dislocations observed at the interface due to very small lattice misfit. The

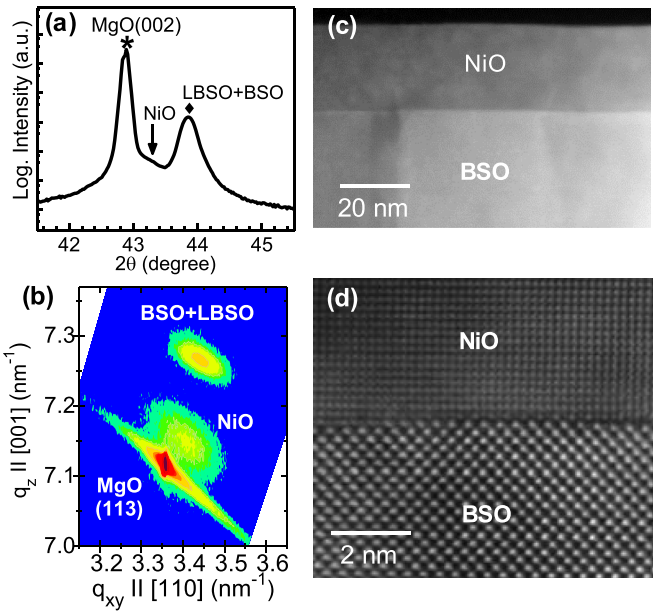


FIG. 3. (a) XRD $\theta$-$2\theta$ scan and (b) RSM of the NiO/BSO heterojunction grown on MgO(001) (* for reflection peaks from MgO and ◆ for peaks from perovskite). (c) and (d) Low-magnified and high-resolution STEM images of the interface region of a NiO/BSO heterojunction, respectively.

interface is sharp without a large amount of interdiffusion at the interface.

We fabricated a simple *p-n* junction diode for the current-voltage (*I-V*) measurement, and the layer structure is shown in Fig. 4(a). The LBSO layer (150 nm thick) was deposited as a transparent electrode. Figure 4(b) shows the *I-V* characteristics measured at room temperature, clearly indicating the rectifying behavior. The rectifying ratio is about 500 at ±3.0 V. High-resolution XPS was used to determine the built-in potential ($V_{bi}$) and valence band offsets ($\Delta E_V$) at the interface. To this end, we deposited thin NiO overlayers with thicknesses of 2 nm and 4 nm on BSO. These thicknesses are still thin enough to allow sufficient photoelectron signals from buried BSO to be measured. The $V_{bi}$ value can be determined from energy shifts of the core-level peak position. Figures 4(c) and 4(d) show Ba $3d_{5/2}$ and Sn $3d_{5/2}$ core level spectra for bare BSO and after deposition of 2 nm and 4 nm NiO films. Both Ba $3d_{5/2}$ and Sn $3d_{5/2}$ core levels shift 0.90 eV to lower BE values. This indicates upward band bending in BSO, as expected due to charge transfer across the *p-n* interface. Likewise, downward band bending (~0.15 eV) is observed in NiO by comparing the Ni $2p_{3/2}$ of the 2 nm overlayer with those of thicker films, as shown in Fig. 4(e).

The $\Delta E_V$ between NiO and BSO can be determined by the method developed by Kraut *et al.*[55,56] using the following equation:

$$\Delta E_V = (E_{Ni2p} - E_{VBM})_{NiO} - (E_{Sn3d} - E_{VBM})_{BSO} - (E_{Ni2p} - E_{Sn3d})_{HJ}$$

where $(E_{Ni2p} - E_{VBM})_{NiO}$ and $(E_{Sn3d} - E_{VBM})_{BSO}$ are the energy differences in the core levels from the respective VBM for NiO and BSO, respectively. These were obtained from 25 nm NiO and 150 nm BSO thick films grown on

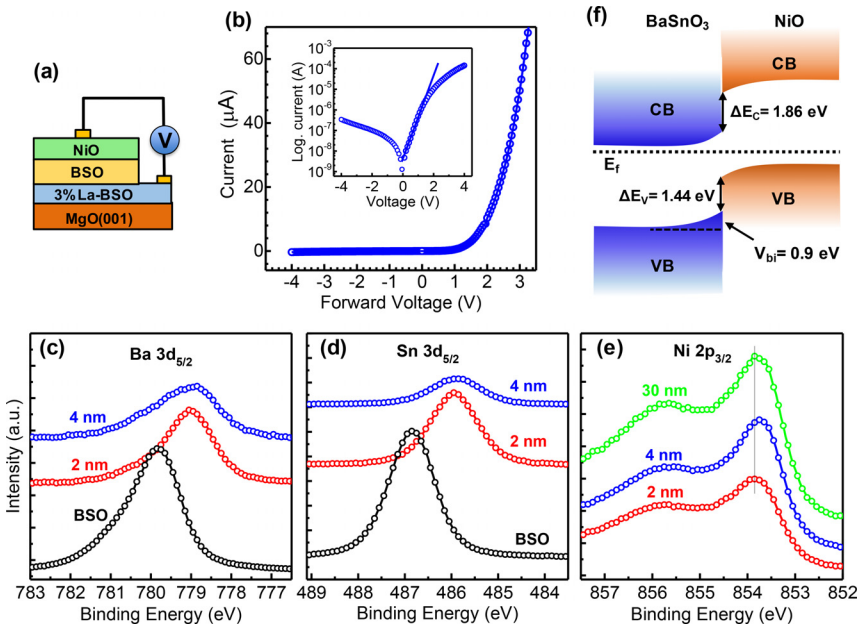


FIG. 4. (a) Schematic structure of the *p-n* heterojunction. (b) Current *vs* voltage characteristics of the *p-n* heterojunction; the inset shows the semi-logarithmic *I-V* curve. (c)–(e) Core levels of Sn $3d_{5/2}$, Ba $3d_{5/2}$ of BSO, and Ni $2p$ of NiO with different NiO ultra-thin film thicknesses, respectively. (f) Energy diagram at the NiO/BSO interface.

MgO. $(E_{Ni2p} - E_{Sn3d})_{HJ}$ is the binding energy (BE) difference between Ni $2p$ and Sn $3d$ for thin NiO overlayers (e.g., 2 nm and 4 nm) on BSO. Furthermore, once $\Delta E_V$ is known, the conduction band offset ($\Delta E_C$) can be readily determined by $\Delta E_C = \Delta E_V + (E_g^{NiO} - E_g^{BSO})$, where $E_g^{NiO}$ is the bandgap of NiO as determined to be ~3.65 eV,[31] and $E_g^{BSO}$ is the bandgap of BSO (3.23 eV, as determined from our measurement). Table S1 (see supplementary material) summarizes the values of the BE difference used to calculate the band offset and the resultant $\Delta E_V$ and $\Delta E_C$ values of the NiO/BSO heterojunctions with 2 nm and 4 nm NiO films. The averaged $\Delta E_V$ and $\Delta E_C$ are 1.44 eV and 1.86 eV, respectively, indicating the formation of type-II staggered band alignment at the interface.[33,57]

Figure 4(f) summarizes the band offsets and built-in potential of the NiO/BSO heterojunction deduced from XPS measurements. Since $\Delta E_V$ (1.44 eV) is less than $\Delta E_C$ (1.86 eV), holes should be the dominant carries across the *p-n* junction under forward bias. In principle, a forward voltage of $V = (V_{bi} + \Delta E_V)/e = 2.49$ V is necessary to overcome the barriers for injecting holes from NiO into BSO. However, the experimental turn-on voltage for our diode is ~1.5 V, as shown in Fig. 4(b). The much lower turn-on voltage indicates the participation of other transport mechanisms. We further fit the *I–V* characteristics using the Shockley equation: $I = I_s[\exp(qV/nkT)-1]$, where $I_s$ is the reverse saturation current, $q$ the electron charge, $k$ the Boltzmann constant, $T$ the temperature, and $n$ the ideality factor, which can be obtained from the slope of the linear part of the semi-logarithmic *I–V* curve. The $n$ for the NiO/BSO heterojunction is determined to be 7.7 in the bias range of 0.1–1.2 eV [inset in Fig. 4(b)]. A large ideality factor ($n > 2.0$) has been observed in several other oxide-based *p-n* heterojunctions. The large ideality factor suggests other charge transport mechanisms such as interface recombination and/or current tunneling assisted by interface states, polar discontinuity, cation interdiffusion, and space-charge-limited conduction.[33,58] Work is underway to optimize the device performance and to gain microscopic mechanism on the transport properties. Nonetheless, our present work show that ordered NiO films can be epitaxially grown on BSO with a well-defined interface. The two materials form "staggered" band alignment with a large built-in potential of up to 0.90 eV in BSO. Such interfacial electronic properties are favorable for the separation and transport of photo-generated electrons and holes. This *p-n* heterojunction could be promising in the application of UV photodetectors.

In summary, we have fabricated transparent *p-n* heterojunctions consisting of NiO and BSO epitaxially grown on MgO(001) substrates by PLD. Our combined optical absorption and XPS valence band measurements are in support of an indirect bandgap value of 3.23 eV for undoped BSO. The transparent *p-n* heterojunction exhibits a large rectification ratio of 500. Detailed XPS measurements indicate that NiO/BSO heterojunctions form a type II band alignment, with a large band bending of 0.90 eV for BSO and ~0.15 eV for NiO. Such electronic properties have important implications for optoelectronic applications as the large built-in potential provides favorable energetics for photo-generated electron-hole separation/migration.

See supplementary material for experimental details and Table S1.

K.H.L. Zhang is grateful for funding support from the Thousand Youth Talents Program of China and Herchel Smith Postdoctoral Fellowship by the University of Cambridge. S. Han, S. Xiang, J. Zou, and M. Gu were supported by the Pico Center at SUSTech that receives support from Presidential fund and Development and Reform Commission of Shenzhen Municipality.

[1]K. Ellmer, Nat. Photonics **6**, 809 (2012).
[2]P. P. Edwards, A. Porch, M. O. Jones, D. V. Morgan, and R. M. Perks, Dalton Trans. **2004**, 2995.
[3]Y. Zeng, H. L. Ning, Z. K. Zheng, H. K. Zhang, Z. Q. Fang, R. H. Yao, M. Xu, L. Wang, L. F. Lan, J. B. Peng, X. B. Lu, and Y. Q. Zheng, Adv. Mater. Interfaces **4**, 1700063 (2017).

[4]Z. Wang, P. K. Nayak, J. A. Caraveo-Frescas, and H. N. Alshareef, Adv. Mater. **28**, 3831 (2016).
[5]S. D. Singh, R. S. Ajimsha, V. Sahu, R. Kumar, P. Misra, D. M. Phase, S. M. Oak, L. M. Kukreja, T. Ganguli, and S. K. Deb, Appl. Phys. Lett. **101**, 212109 (2012).
[6]K. Baraik, S. D. Singh, Y. Kumar, R. S. Ajimsha, P. Misra, S. N. Jha, and T. Ganguli, Appl. Phys. Lett. **110**, 191603 (2017).
[7]S. Y. Smolin, A. K. Choquette, R. G. Wilks, N. Gauquelin, R. Félix, D. Gerlach, S. Ueda, A. L. Krick, J. Verbeeck, M. Bär, J. B. Baxter, and S. J. May, Adv. Mater. Interfaces **4**, 1700183 (2017).
[8]L. Qiao, W. Li, H. Xiao, H. M. Meyer, X. Liang, N. V. Nguyen, W. J. Weber, and M. D. Biegalski, ACS Appl. Mat. Interfaces **6**, 14338 (2014).
[9]M. Grundmann, R. Karsthof, and H. von Wenckstern, ACS Appl. Mat. Interfaces **6**, 14785 (2014).
[10]W. J. Lee, H. J. Kim, J. Kang, D. H. Jang, T. H. Kim, J. H. Lee, and K. H. Kim, Annu. Rev. Mater. Res. **47**, 391 (2017).
[11]A. Prakash, P. Xu, A. Faghaninia, S. Shukla, J. W. Ager III, C. S. Lo, and B. Jalan, Nat. Commun. **8**, 15167 (2017).
[12]H.-R. Liu, J.-H. Yang, H. J. Xiang, X. G. Gong, and S.-H. Wei, Appl. Phys. Lett. **102**, 112109 (2013).
[13]S. Dabaghmanesh, R. Saniz, M. N. Amini, D. Lamoen, and B. Partoens, J. Phys.: Condens. Matter **25**, 415503 (2013).
[14]K. Krishnaswamy, L. Bjaalie, B. Himmetoglu, A. Janotti, L. Gordon, and C. G. Van de Walle, Appl. Phys. Lett. **108**, 083501 (2016).
[15]H. J. Kim, U. Kim, T. H. Kim, J. Kim, H. M. Kim, B.-G. Jeon, W.-J. Lee, H. S. Mun, K. T. Hong, J. Yu, K. Char, and K. H. Kim, Phys. Rev. B **86**, 165205 (2012).
[16]H. J. Kim, U. Kim, H. M. Kim, T. H. Kim, H. S. Mun, B.-G. Jeon, K. T. Hong, W.-J. Lee, C. Ju, K. H. Kim, and K. Char, Appl. Phys. Express **5**, 061102 (2012).
[17]D. J. Singh, D. A. Papaconstantopoulos, J. P. Julien, and F. Cyrot-Lackmann, Phys. Rev. B **44**, 9519 (1991).
[18]D. O. Scanlon, Phys. Rev. B **87**, 161201 (2013).
[19]J. H. Lee, W. J. Lee, T. H. Kim, T. Lee, S. Hong, and K. H. Kim, J. Phys.: Condens. Matter **29**, 384004 (2017).
[20]B. C. Luo, J. Wang, X. S. Cao, and K. X. Jin, Phys. Status Solidi A **211**, 705 (2014).
[21]H. M. Kim, U. Kim, C. Park, H. Kwon, and K. Char, APL Mater. **4**, 056105 (2016).
[22]K. Fujiwara, K. Nishihara, J. Shiogai, and A. Tsukazaki, AIP Adv. **6**, 085014 (2016).
[23]U. Kim, C. Park, T. Ha, Y. M. Kim, N. Kim, C. Ju, J. Park, J. Yu, J. H. Kim, and K. Char, APL Mater. **3**, 036101 (2015).
[24]J. Shin, Y. M. Kim, Y. Kim, C. Park, and K. Char, Appl. Phys. Lett. **109**, 262102 (2016).
[25]S. S. Shin, E. J. Yeom, W. S. Yang, S. Hur, M. G. Kim, J. Im, J. Seo, J. H. Noh, and S. I. Seok, Science **356**, 167 (2017).
[26]S. A. Chambers, T. C. Kaspar, A. Prakash, G. Haugstad, and B. Jalan, Appl. Phys. Lett. **108**, 152104 (2016).
[27]T. S. Tripathi and M. Karppinen, Adv. Mater. Interfaces **4**, 1700300 (2017).
[28]H. Sato, T. Minami, S. Takata, and T. Yamada, Thin Solid Films **236**, 27 (1993).
[29]R. K. Gupta, K. Ghosh, and P. K. Kahol, Physica E **41**, 617 (2009).
[30]J. Y. Zhang, W. W. Li, R. L. Z. Hoye, J. L. MacManus-Driscoll, M. Budde, O. Bierwagen, L. Wang, Y. Du, M. J. Wahila, L. F. J. Piper, T.-L. Lee, H. J. Edwards, V. R. Dhanak, and K. H. L. Zhang, J. Mater. Chem. C **6**, 2275 (2018).
[31]K. H. L. Zhang, R. Wu, F. Tang, W. Li, F. E. Oropeza, L. Qiao, V. K. Lazarov, Y. Du, D. J. Payne, J. L. MacManus-Driscoll, and M. G. Blamire, ACS Appl. Mat. Interfaces **9**, 26549 (2017).
[32]C. C. Wu and C. F. Yang, ACS Appl. Mat. Interfaces **5**, 4996 (2013).
[33]M. Grundmann, F. Klüpfel, R. Karsthof, P. Schlupp, F.-L. Schein, D. Splith, C. Yang, S. Bitter, and H. von Wenckstern, J. Phys. D: Appl. Phys. **49**, 213001 (2016).
[34]R. Karsthof, H. von Wenckstern, and M. Grundmann, IEEE Trans. Electron Devices **62**, 3999 (2015).
[35]H. Ohta, M. Hirano, K. Nakahara, H. Maruta, T. Tanabe, M. Kamiya, T. Kamiya, and H. Hosono, Appl. Phys. Lett. **83**, 1029 (2003).
[36]S. Liu, R. Liu, Y. Chen, S. Ho, J. H. Kim, and F. So, Chem. Mater. **26**, 4528 (2014).
[37]R. D. Shannon, Acta Crystallogr., Sect. A **32**, 751 (1976).
[38]Q. Liu, J. Liu, B. Li, H. Li, G. Zhu, K. Dai, Z. Liu, P. Zhang, and J. Dai, Appl. Phys. Lett. **101**, 241901 (2012).
[39]H. Mizoguchi, H. W. Eng, and P. M. Woodward, Inorg. Chem. **43**, 1667 (2004).
[40]Z. Lebens-Higgins, D. O. Scanlon, H. Paik, S. Sallis, Y. Nie, M. Uchida, N. F. Quackenbush, M. J. Wahila, G. E. Sterbinsky, D. A. Arena, J. C. Woicik, D. G. Schlom, and L. F. Piper, Phys. Rev. Lett. **116**, 027602 (2016).
[41]S. Sallis, D. O. Scanlon, S. C. Chae, N. F. Quackenbush, D. A. Fischer, J. C. Woicik, J. H. Guo, S. W. Cheong, and L. F. J. Piper, Appl. Phys. Lett. **103**, 042105 (2013).
[42]K. Ganguly, P. Ambwani, P. Xu, J. S. Jeong, K. A. Mkhoyan, C. Leighton, and B. Jalan, APL Mater. **3**, 062509 (2015).
[43]K. Ganguly, A. Prakash, B. Jalan, and C. Leighton, APL Mater. **5**, 056102 (2017).
[44]P. Singh, B. J. Brandenburg, C. P. Sebastian, P. Singh, S. Singh, D. Kumar, and O. Parkash, Jpn. J. Appl. Phys., Part 1 **47**, 3540 (2008).
[45]E. Burstein, Phys. Rev. **93**, 632 (1954).
[46]K. H. L. Zhang, R. G. Egdell, F. Offi, S. Iacobucci, L. Petaccia, S. Gorovikov, and P. D. C. King, Phys. Rev. Lett. **110**, 056803 (2013).
[47]W. Zhang, J. Tang, and J. Ye, J. Mater. Res. **22**, 1859 (2011).
[48]D. J. Singh, Q. Xu, and K. P. Ong, Appl. Phys. Lett. **104**, 011910 (2014).
[49]K. H. L. Zhang, K. Xi, M. G. Blamire, and R. G. Egdell, J. Phys.: Condens. Matter **28**, 383002 (2016).
[50]K. H. L. Zhang, Y. G. Du, A. Papadogianni, O. Bierwagen, S. Sallis, L. F. J. Piper, M. E. Bowden, V. Shutthanandan, P. V. Sushko, and S. A. Chambers, Adv. Mater **27**, 5191 (2015).
[51]R. L. Weiher and R. P. Ley, J. Appl. Phys. **37**, 299 (1966).
[52]P. Erhart, A. Klein, R. G. Egdell, and K. Albe, Phys. Rev. B **75**, 153205 (2007).
[53]A. Walsh, J. L. Da Silva, S. H. Wei, C. Korber, A. Klein, L. F. Piper, A. DeMasi, K. E. Smith, G. Panaccione, P. Torelli, D. J. Payne, A. Bourlange, and R. G. Egdell, Phys. Rev. Lett. **100**, 167402 (2008).
[54]K. H. L. Zhang, V. K. Lazarov, T. D. Veal, F. E. Oropeza, C. F. McConville, R. G. Egdell, and A. Walsh, J. Phys.: Condens. Matter **23**, 334211 (2011).
[55]E. A. Kraut, R. W. Grant, J. R. Waldrop, and S. P. Kowalczyk, Phys. Rev. Lett. **44**, 1620 (1980).
[56]E. A. Kraut, R. W. Grant, J. R. Waldrop, and S. P. Kowalczyk, Phys. Rev. B **28**, 1965 (1983).
[57]A. Giampietri, G. Drera, and L. Sangaletti, Adv. Mater. Interfaces **4**, 1700144 (2017).
[58]F. L. Schein, H. von Wenckstern, and M. Grundmann, Appl. Phys. Lett. **102**, 092109 (2013).